RESEARCH ARTICLE

WILEY

Gyral peaks: Novel gyral landmarks in developing macaque brains

Songyao Zhang[1] | Poorya Chavoshnejad[2] | Xiao Li[3] | Lei Guo[1] | Xi Jiang[4] | Junwei Han[1] | Li Wang[5] | Gang Li[5] | Xianqiao Wang[6] | Tianming Liu[7] | Mir Jalil Razavi[2] | Shu Zhang[8] | Tuo Zhang[1]

[1]School of Automation, Northwestern Polytechnical University, Xi'an, China

[2]Department of Mechanical Engineering, State University of New York at Binghamton, New York, USA

[3]School of Information Technology, Northwest University, Xi'an, China

[4]School of Life Science and Technology, University of Electronic Science and Technology of China, Chengdu, China

[5]Department of Radiology and BRIC, University of North Carolina at Chapel Hill, Chapel Hill, North Carolina, USA

[6]College of Engineering, The University of Georgia, Athens, Georgia, USA

[7]Cortical Architecture Imaging and Discovery Lab, Department of Computer Science and Bioimaging Research Center, The University of Georgia, Athens, Georgia, USA

[8]Center for Brain and Brain-Inspired Computing Research, Department of Computer Science, Northwestern Polytechnical University, Xi'an, China

Correspondence
Tuo Zhang, School of Automation Northwestern Polytechnical University Xi'an, China.
Email: tuozhang@nwpu.edu.cn

Abstract

Cerebral cortex development undergoes a variety of processes, which provide valuable information for the study of the developmental mechanism of cortical folding as well as its relationship to brain structural architectures and brain functions. Despite the variability in the anatomy–function relationship on the higher-order cortex, recent studies have succeeded in identifying typical cortical landmarks, such as sulcal pits, that bestow specific functional and cognitive patterns and remain invariant across subjects and ages with their invariance being related to a gene-mediated proto-map. Inspired by the success of these studies, we aim in this study at defining and identifying novel cortical landmarks, termed gyral peaks, which are the local highest foci on gyri. By analyzing data from 156 MRI scans of 32 macaque monkeys with the age spanned from 0 to 36 months, we identified 39 and 37 gyral peaks on the left and right hemispheres, respectively. Our investigation suggests that these gyral peaks are spatially consistent across individuals and relatively stable within the age range of this dataset. Moreover, compared with other gyri, gyral peaks have a thicker cortex, higher mean curvature, more pronounced hub-like features in structural connective networks, and are closer to the borders of structural connectivity-based cortical parcellations. The spatial distribution of gyral peaks was shown to correlate with that of other cortical landmarks, including sulcal pits. These results provide insights into the spatial arrangement and temporal development of gyral peaks as well as their relation to brain structure and function.

Shu Zhang and Tuo Zhang are joint correspondence authors.

1 | INTRODUCTION

Cerebral cortex folds during its development in most mammalian brains (Rakic 2009, Sun and Hevner 2014). It has been widely reported that normal cortical growth and folding patterns are crucial for normal brain function since abnormality in cortical folding induced by aberrant or interrupted neuronal development has been related to many brain function malformations, cognitive deficits, and mental disorders (Richman et al. 1974, Clark 2001, Molko et al. 2003, Gaitanis and Walsh 2004, Rakic 2004, Nakamura et al. 2007, Cykowski et al. 2008, Shim et al. 2009, Barkovich et al. 2012, Stutterd and Leventer 2014, Fernández et al. 2016, Di Donato et al. 2017). Therefore, it has long been a wide interest in estimating a precise and consistent mapping of brain anatomy to cyto- and myelo- architectures, and functional activities (Zilles and Palomero-Gallagher 2001).

However, the high variability of cortical folding patterns presents huge challenges for estimating the brain anatomy-function relationship. Even the primary sulci and gyri, which can be consistently identified in all the healthy individuals and have a clear relation to major function areas, were demonstrated to not align very well with boundaries of a finer functional/cytoarchitectonic subdivision (Rademacher et al. 1993, Zilles et al. 1997, Roland and Zilles 1998, Amunts et al. 2000, Hasnain et al. 2001, Morosan et al. 2001, Eickhoff et al. 2006, Fischl et al. 2008, Hinds et al. 2008, Frost and Goebel 2012), let alone the secondary/tertiary gyri and sulci for which it is even difficult to find anatomical cross-individual correspondence due to their huge variability (Ono et al. 1990).

Therefore, the identification of cortical landmarks that bear higher anatomical cross-individual consistency and more consistent relation to functional areas at a finer resolution than the coarse-resolution folding patterns, such as gyri and sulci (Jiang et al. 2021) could improve the accuracy of anatomy-function mapping (Lohmann et al. 2008).

In fact, many cortical landmarks have been found and demonstrated to satisfy these requirements. In sulcal regions, it has been demonstrated that the sulcal patterns become more consistent at increasing depths (Le Goualher et al. 1999, Lohmann et al. 1999). The locally deepest sulcal foci, also known as sulcal pits, could be the first putative cortical folds present at the fetal stage (Im et al. 2017). Their location and geometry are relatively stable across individuals and change least as the brain develops (Lohmann et al. 2008, Im et al. 2010, Im et al. 2011, Meng et al. 2014). The invariance was further associated with the regulative effects of genetic control (McKay et al. 2013, Le Guen et al. 2018). Importantly, the presence/absence of sulcal pits has been demonstrated to relate to brain function and cognition. For example, the hemispheric asymmetries of sulcal pits distribution and frequency on superior temporal sulcus were related to the lateralization of language function in human brains in both infant and adult groups (Im et al. 2010). The presence of sulcal pit in the left posterior inferior frontal sulcus and the right posterior inferior temporal sulcus is related to verbal intelligence (Im et al. 2011). The number of sulcal pits in the left posterior inferior frontal sulcus and the right posterior inferior temporal sulcus was positively related to average IQ

(Im et al. 2013). Also, sulcal patterns on postnatal brains with cerebral malformation are significantly different from normal templates regarding the location and depth (Im et al. 2017).

Despite these insightful and promising findings in sulcal regions, few studies were found to identify whether there are similar cortical landmarks in gyral system. In fact, gyri and sulci develop simultaneously in the same cortical regions. For example, sylvian fissure and insular gyrus develop at 10 ∼ 15 gestation week (GW), and the central sulcus that develops at 20 ∼ 23 GW is followed by the development of precentral gyrus and postcentral gyrus at 24–27 GW (Chi et al. 1977, Welker 1990, Zilles et al. 1997, Blanton et al. 2001, White et al. 2010). Importantly, the presence/absence of a gyrus could also be related to brain function or even cognitive capacity. For example, it was reported that adults whose left lateral occipitotemporal sulcus were interrupted by the gyrus in the posterior portion had better reading fluency than those having a continuous one (Cachia et al. 2018). In this sense, we intuitively wonder whether a cortical landmark, as a possible counterpart of a sulcal pit, can be found in gyral regions.

To this end, we defined gyral peaks as the locally highest points along gyral crests, developed a computational method for extracting gyral peaks, and examined their spatial distribution, longitudinal variation, and relationship to structural connectivity parcellation based on a longitudinal neuroimaging of the rhesus macaque brains dataset (Young et al. 2017). Fewer inter-individual and temporal variabilities in cortical folding of macaque brains than those of human brains could assist us to estimate the spatiotemporal alignment of cortical folds (including gyral peaks in this work) across subjects and/or ages, and the mapping of structural/functional architectures to gyral peaks, with higher accuracy. In this dataset, we investigated whether gyral peaks are spatially consistent across individuals and ages; whether they bear identifiable anatomical, structural connective and functional features compared to other gyral regions; and how are they related to sulcal pits. In all these respects, we considered that the gyral peaks, the locally highest points of a gyral crest, are the significant gyral landmarks.

2 | METHODS

2.1 | Dataset

Thirty-two healthy rhesus macaques used in this study were obtained from the University of Wisconsin-Madison dataset (Young et al. 2017). Each subject has four or five longitudinal brain MRI scans (GE MR750 3.0 T) at scheduled intervals, resulting in a total of 156 scans (scanning schedule in Figure S1). The parameters of T1-weighted MRI are as follows: TI = 450 ms, TR = 8.684 ms, TE = 3.652 ms, FOV = 140×140 mm^2, flip angle = 12 deg, thickness = 0.8 mm, gap = −0.4 mm, 80% field-of-view in phase encoding direction, bandwidth = 31.25 kHz, 2 averages, total time = 10:46 min, acquisition matrix = 256×256 and voxel size = $0.55 \times 0.55 \times 0.8$ mm^3. The parameters of diffusion MRI are

as follows: TR = 8000 ms, TE = 65.7 ms, FOV = 16.7 mm, matrix = 128 × 128, slice thickness = 2.6 mm, with 1.3 mm slice overlap (resolution 1.3 × 1.3 × 2.6 mm^3), up-sampled to a voxel dimension on the scanner of 0.65 × 0.65 × 1.3 mm^3, 120 gradient directions with b = 1000s/mm^2 and 10 images with b = 0 s/mm^2.

2.2 | Data preprocessing

For structural MRI, we adopted an infant-specific computational pipeline (Wang et al. 2018, Xia et al. 2020). A bias field correction for the T1 and T2 images, respectively, was applied using the N4 method (Tustison et al. 2010). Then, we rigidly registered all T2-weighted images to their corresponding T1-weighted images and resampled all images to be isotropic with the resolution of 0.55 × 0.55 × 0.55 mm^3. After removing the skull, brain stem, and cerebellum (Zhong et al. 2021), we used an infant-dedicated learning-based method, coupled with longitudinal guidance (Wang et al. 2013, 2014, 2015) to perform brain tissue segmentation (white matter, WM; gray matter, GM; cerebrospinal fluid, CSF). On the segmentation result, we reconstructed the inner (WM) and outer (GM) cortical surfaces by using the method in Li et al. (2012, 2014) and have the surface topology corrected (Sun et al. 2019). For dMRI, we performed skull-strip and eddy current correction via FSL (Jenkinson et al. 2012, Andersson and Sotiropoulos 2016). DSI-Studio was used to estimate the voxel-wise distribution of water diffusion (Yeh et al. 2010) and track 4 × 10^4 deterministic fibers for the whole-brain (Yeh et al. 2013) with default parameters (max turning angle: 60 deg, streamline length: 30 mm-300 mm, step length: 1 mm, and quantitative anisotropy threshold: 0.2).

2.3 | Gyral height and gyral peaks

As shown in Figure 1a-b, gyral height and gyral peaks were defined in an individual surface. We used morphological opening operations with a spherical structuring element of radius 6 mm in the WM map to yield the "opened surface" (the red closed curves in Figure 1a), which is "a deep white matter surface resembling a primitive unfolded or lissencephalic brain" as described in Lohmann et al. (2008). Discussion on the selection of radius as well as the selection on different ages is present in section 3.1 and Supplemental Materials (Figure S2 and related texts). To measure the height of a vertex on the white matter surface, we adopted the algorithm named the adaptive distance transform (ADT) (Jin et al. 2013) to compute the length of the shortest path that is within white matter from the vertex to the opened surface (curves in gyri in Figure 1a). In this way, we obtained the gyral height surface map (right panel of Figure 1a). For the convenience of analyses across subjects, we normalize the height to [0, 1]. We defined the vertex with local maximal gyral height value in 9-order ring neighbors (radius is about 2.34 mm) as a gyral peak center (the yellow bubble in Figure 1b). The X-order ring neighbors of a vertex include the vertices that are X-steps away on the triangular mesh. For ease of
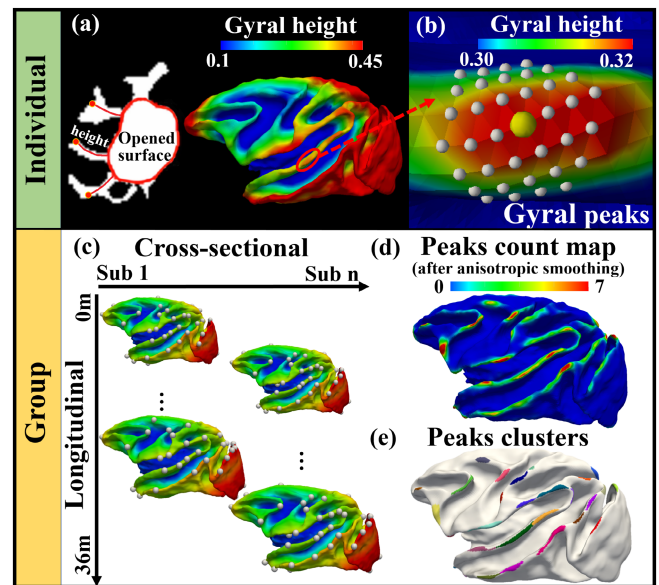

FIGURE 1 The preprocessing pipeline. (a-b) were performed in individual spaces. (c-e) were performed on the cohort. (a) Definitions of gyral height. Left: Morphological opening operation was applied to white matter regions to yield an opened surface (red closed curve). Gyral height of a vertex on the WM surface is defined as the length of the shortest path that is within white matter from the vertex to the opened surface (red curves). The height of each subject has been normalized to the range between 0 and 1. Right: Gyral height map on the white matter surface. These steps were conducted on each session of each subject, respectively. (b) the vertex with local maximal gyral height (yellow bubble) as well as its 3-order ring neighbor vertices (white bubbles) were defined as a gyral peak. Gyral height map was rescaled to highlight the location of the local maximum. (c) Vertex-to-vertex correspondences among all surfaces were used for the construction of group-wise gyral peak count map in (d). White bubbles in (c) highlight the locations of gyral peaks in individual spaces. It is noted that the map in (d) encodes both inter-individual and longitudinal variabilities. The count map in (d) was smoothed and capped to [0, 7] for convenience of presentation. (e) Gyral peak clusters obtained by watershed clustering algorithm (Meng et al. 2014)

analysis in the following steps (such as cross-subject smoothing), a gyral peak is defined as the peak center and its local neighbors (vertices within a 3-order ring highlighted by white dots in Figure 1b). It is noted that identification of local height maxima is not impacted by the normalization of height (to [0, 1]).

2.4 | Gyral peak count maps and group-wise clusters

As shown in Figure 1c, longitudinal (intra-subject) cortical correspondences were established by aligning longitudinal surfaces and generating the mean intra-subject cortical folding map via spherical demons (Yeo et al. 2009). Cross-sectional (inter-subject) correspondences were established by aligning all the intra-subject mean cortical folding

maps and generating the group-mean cortical folding maps. We resampled the aligned cortical surfaces to a standard-mesh tessellation with 160 K vertices, establishing vertex-to-vertex correspondences across the cohort (Xia et al. 2020).

To conduct group-wise analysis, we randomly selected a surface (the one in Figure 1d) as the template surface and mapped the gyral peaks in individual spaces (white bubbles in Figure 1c) to it. On this template surface, we counted for each vertex how many gyral peaks from all surfaces are overlaid on it and produced a count map.

The anisotropic smooth algorithm with 20 iterations and mask size of 7-order ring neighborhood were applied to the count map (Meng et al. 2014). The final count map is shown in Figure 1d. We adopted a watershed clustering algorithm (Rettmann et al. 2002, Yang and Kruggel 2008, Meng et al. 2014) to determine the number and the location of peak clusters on the count map (Figure 1e). Since each cluster has only one maximum, the location of the maximum was used as the location of the group-wisely consistent peak for this cluster.

It is noted that the group-wise analysis shown in Figure 1 was applied to all 156 sessions. To investigate temporal changes in these gyral peaks, we divided the 156 individuals into four age groups (0–6 months, 7–15 months, 16–24 months, and 28–36 months). The same analysis pipeline was applied to each age group, respectively.

2.5 | Anatomical and structural measures

We used vertex-wise cortical thickness and mean curvature on surfaces to measure the morphology of the cortex. Cortical thickness was defined as the shortest Euclidean distance from the vertex on the white matter surface to the gray matter surface.

For white matter structural connective metrics, we constructed a structural connective graph $G = \{V, E, A\}$ for each session of each subject. The white matter surface was parcellated into 1000 patches of the same area, which were used as nodes $v_i s \in V$ (Zhang et al. 2020). It is noted that we excluded the regions between two hemispheres before parcellation. An edge e_{ij} in E was defined as the dMRI fiber tracts, if any, that connected v_i and v_j. a_{ij} in A is the attribute associated with edge e_{ij}. It is defined as the connective strength, that is, the number of fiber tracts that link v_i and v_j (Van Den Heuvel and Sporns 2011, Van Den Heuvel et al. 2012). On this graph, we computed nodal graph metrics, including degree, strength, betweenness, and efficiency, via Brain Connectome Toolkit (https://sites.google.com/site/bctnet/). Since we are particularly interested in gyral peaks, a surface patch where a gyral peak resides was regarded as a gyral peak node. It is noted that only 60 dMRI scans with high deterministic fiber quality (manually checked by an expert) were used to derive structural connective metrics (data distribution in Figure S3).

In addition to dMRI derived connections, we adopted the brain atlas in Lewis and Van Essen (2000) (LVE atlas for short), which used retrograde tracers to identify input and output of anatomical connection on cortex as well as their cortical borders. LVE atlas is available at the F99 macaque surface template (Van Essen 2002, Van Essen and

Dierker 2007). Since the template and the atlas are developed on adult macaque brains, we only transfer them to the scans in the fourth age group of our study (28–36 months) by means of spherical surface registration method (Yeo et al. 2009).

3 | RESULTS

3.1 | Parameter selection and reproducibility

The radius of the spherical structuring element in opening operations on the WM volumetric map is set as $r = 6$ mm. The criterion is visually examining that if the opened surface touches the fundi of all major sulci and if the detected peaks are representative ones. Variation in brain size is also considered when $r = 6$ mm is selected. Details are found in Figure S2, Table S1, and related texts in Supporting Information. We chose 9-order ring neighbors (radius is about 2.34 mm) as the search range of local maxima (peaks) on the height map. 9-order ring search scope for the four age groups is 2.23 ± 0.12 mm, 2.30 ± 0.08 mm, 2.34 ± 0.10 mm and 2.37 ± 0.09 mm. Moreover, we compared the method using 9-order ring search scope with the method using spherical masks. The yielded peaks and count maps are similar. The details are reported in the Supplemental Materials (section 4.2). Indeed, we compared the results using different search ranges (6- to 11-order ring neighbors) and found that different choice has little effect on the results. Details are found in Figure S4 and related texts in Supporting Information. We chose 7-order ring plus iteration = 20 for anisotropic smooth algorithm. Indeed, we compared count maps and peak clusters using different smooth mask sizes (5- to 13-order ring neighbors) or different iterations (10–28 iterations). Details are found in Figure S6, Table S4, and related texts in Supporting Information. In general, these results demonstrate the insensitivity of count map smoothing and cluster generation to either smooth sizes or iterations, and the robustness of the following results based on size = 7-order ring and iteration = 20. Parameters for watershed clustering were manually adjusted for the all-age group (Figure 1d) till all clusters (but not noise) on the count maps were isolated by visual inspection. Since we also generated clusters in different age groups, the parameters for watershed clustering were slightly manually adjusted based on those used for the all-age results. Likewise, visual inspection was used to ensure that the clusters were well isolated in each age group, respectively.

Finally, we applied the peak identification pipeline and the selected parameters to an independent dataset, the UC-Davis dataset (http://fcon_1000.projects.nitrc.org/indi/PRIME/ucdavis.html). Since this dataset only includes adult subjects, we compared the identified group-wise peaks with those in the fourth age group in UNC dataset. The peak overlap ratio (Dice ratio) between the two datasets is 74.28%, demonstrating the reproducibility of the pipeline on another dataset. Dice Ratio was defined as the number of overlapped peaks divided by the total number of peaks on two datasets. Peak correspondence was estimated by searching for the closest paired ones (if distance between them is less than 9-order ring neighborhood,

r ≈ 2.34 mm). More details are found in Section 7 of Supplemental Materials.

3.2 | Spatial distribution of gyral peaks

Figure 2a shows the detected gyral peaks in the individual space of a randomly selected subject. The group-wise peak count map on the template subject was shown in Figure 2b. It is observed that the gyral peaks extracted from all subjects over ages are not scattered on the template but yield a Gaussian distribution in terms of peak count on the template, with the furthest distance of the 95% confidence interval boundaries from the possible centers as 0.95 ± 0.61 mm, on average. Also, the distribution patterns of the distance of two neighboring peaks are similar across subjects (Pearson's r = 0.86 ± 0.14, details are referred to section 5.1 in Supplemental Materials). The gyral peak clusters by applying a watershed algorithm to the count map were shown in Figure 2c. The left and right hemispheres have 39 and 37 clusters, respectively. The count map was further validated via bootstrapping statistics. One-hundred bootstrapping tests yield count maps that have Pearson's r = 0.99 ± 0.15, on average (details are referred to section 5.2 in the Supplemental Materials). The spatial distributions and peak count of most clusters show hemispherical symmetry with four exceptions, including postcentral gyrus, inferior
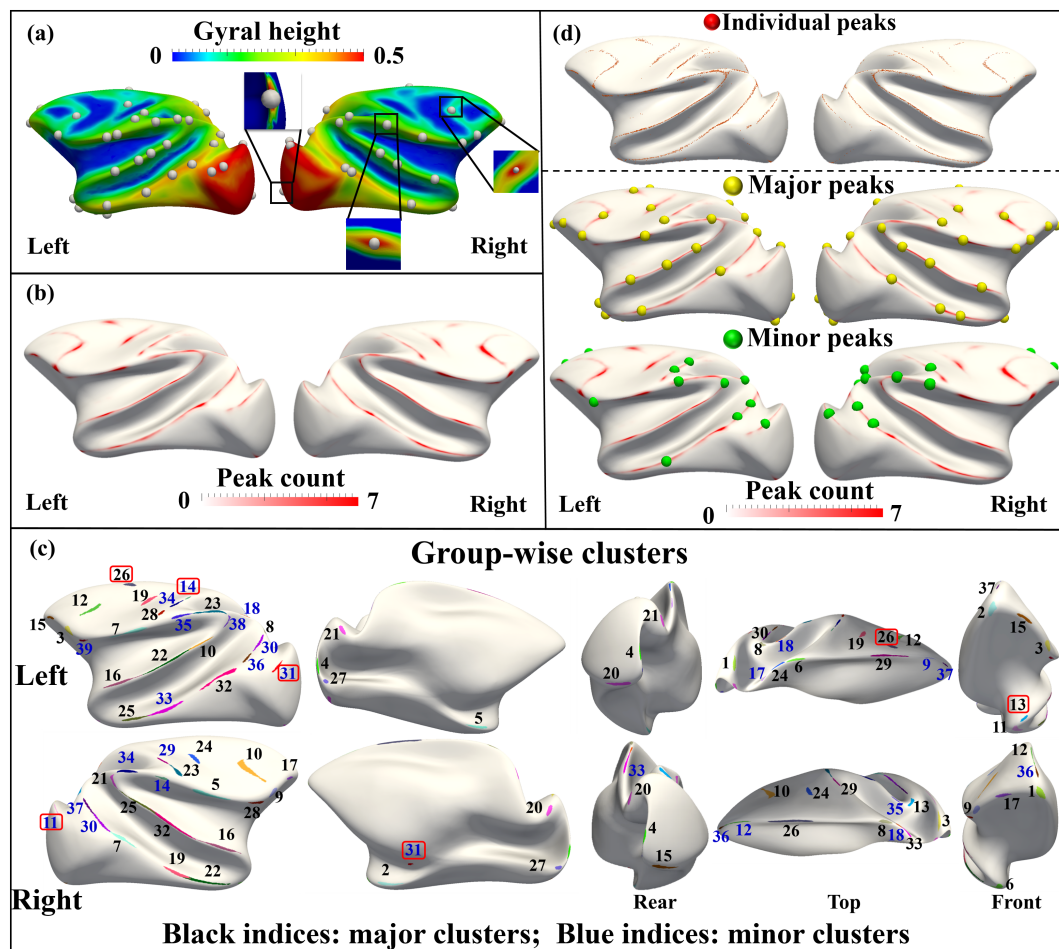

FIGURE 2 (a) Extraction of gyral peaks on an individual surface. Inflated surfaces are color coded by gyral height. White bubbles highlight the locations of local maxima. Gyral heights in three insets are rescaled to better visualize local maxima. (b) Count map of gyral peaks from all subjects and all ages (all scans) on the template surface after anisotropic smoothing and rescaling. Section 5.3 of supplemental materials provides an investigation on peaks and counts on the ventral inferior part of V1/V2 borders. (c) Thirty-nine gyral peaks were identified in left hemisphere from the count map and thirty-seven in right hemisphere, including: (L-9, 29, 37, R-12, 26, 36) superior frontal gyrus; (L-12, 26, R-10) middle frontal gyrus; (L-2, 15, R-1, 17) inferior frontal gyrus; (L-3, 7, 19, 39, R-5, 9, 24, 28) precentral gyrus; (L-14, 28, 34, R-23, 29) postcentral gyrus; (L-6, R-8) superior parietal lobule; (L-23, 35, R-14, 34) inferior parietal lobule; (L-10, 16, 22, 38, R-16, 21, 25, 32) superior temporal gyrus; (L-5, 11, 13, 25, R-2, 6, 22) inferior temporal gyrus; (L-32, 33, R-7, 19) medial inferior temporal gyrus; (L-8, 17, 18, 24, 30, 36, R-13, 18, 30, 37, 33, 35) Occipitotemporal area; (L-21, R-20) cuneus; (L-1, 4, 20, 27, 31, R-3, 4, 11, 15, 27) visual cortex; and (R-31) hippocampal fissure. Red frames highlight the clusters that are not symmetric between hemispheres. (d) Top: All gyral peaks from all scans were mapped to the template surface. Middle and bottom: These peaks were further classified into the more consistent ones (defined as "major peaks", black indices) and the less consistent ones ("minor peaks", blue indices). The centers of these clusters (with the maximal count) were shown against the count map background

temporal gyrus and visual cortex on the left hemisphere and hippocampal fissure on the right hemisphere (framed by red in Figure 2c). The symmetry was supported by the results that the Dice ratio between clusters on the right hemispheres and those mirror-flipped ones from the left hemisphere is 0.53 ± 0.17, in terms of surface area; and the asymmetry index (*AI*) (Greve et al. 2013) between left–right clusters defined as: $AI = (L-R)/(L+R)$, in terms of count density, is $0.16 ± 7.28 \times 10^{-2}$. Details are referred to section 6 in Supplemental Materials. Since peaks with higher count values are those more consistently found across subjects and ages, we investigated whether the consistency is relevant to anatomical and structural measures in the following analyses, by classifying peaks into the more consistent ones (defined as "major peaks", black indices in Figure 2c) and the less consistent ones ("minor peaks", blue indices). We calculated the sum of peak counts in each cluster and arranged them in descending order. Major peak clusters account for 75% counts, leaving the others as minor ones. The left hemisphere has 26 major gyral peaks and 13 minor gyral peaks. The right hemisphere has 25 major gyral peaks and 12 minor gyral peaks. From each gyral peak cluster, we selected the vertex with the highest count as the location of the group-wise gyral peak (Figure 2d).

Finally, to investigate the consistency of major peaks and minor peaks between individuals, we take all major peaks as a group and compute the ratio of the present major peak for the ith individual as follows: $r_i = n_i/n$, where n_i denotes the number of the present major peak on the ith individual and n is the number of major peaks the individual is supposed to have (left hemisphere: $n = 26$; right hemisphere: $n = 25$). A similar ratio was also computed for the minor peak group for the ith individual (13 left minor peaks and 12 right ones are expected). The standard deviation (as well as the mean) of the ratios across individuals are LH (left hemisphere): 0.75 ± 0.08, RH (right hemisphere): 0.75 ± 0.06 for major peaks, and LH: 0.32 ± 0.12, RH: 0.30 ± 0.13 for minor peaks. It is seen that major peaks have less standard deviation than minor peaks, demonstrating the higher cross-individual consistency of major peaks.

3.3 | Comparison across ages

The cluster of gyral peaks obtained on four age groups (0-6 months, 7-15 months, 16-24 months, and 28-36 months) were shown in Figure 3. It is noted that we used the same template in Figure 2 to present the results for ease of comparison. The correspondences of the clusters across age groups were estimated by the overlap ratio between the age-specific cluster map in Figure 3 and the all-age cluster map in Figure 2d which is also shown in the top row of Figure 3 as a reference.

In general, the consistency regarding the spatial distribution of the gyral peak clusters across ages is observed in Figure 3, suggesting that the positions of gyral peaks were considerably independent of the dynamic cortex development, such as tangential cortical expansion and radial height increase. It is noted that a few clusters on the all-age map are not found in one or two age groups (highlighted by red indices and circles in Figure 3).

3.4 | Anatomical and structural attributes of gyral peaks

In this section, we firstly investigated the anatomical and structural features of the more consistent gyral peaks, major peaks in sections 3.4.1 and 3.4.2. Minor peaks, the less consistent ones, were compared with major ones in section 3.4.3.

3.4.1 | Anatomical features

We computed anatomical measures, including cortical thickness and mean curvature, of major gyral peaks at different age groups. Vertices of the same number of peaks were randomly selected and have these anatomical measures computed as well. Random tests were repeated 10,000 times to provide the chance line. Two strategies of random selection were used: 1) random selection on the whole cortex and 2) random selection on gyral crests (curvature>0.5). The mean (±standard deviation) values were reported in Table 1. In general, whether compared to random selection on the whole cortex or gyral crests, major gyral peaks have significantly ($p < .05$ for all) greater thicker cortex and larger curvature.

It is important to note that the significant difference mentioned above is found for all four age groups. The longitudinal comparison reveals that the cortical thickness (L: −17.76 ± 9.72%; R: −15.41 ± 8.48%) and curvature (L: −4.22 ± 9.89%; R: −7.33 ± 11.26%) decreases.

3.4.2 | Structural wiring patterns

As a reference, the mean nodal metrics averaged over random tests on the cortex and gyral crests within each age group were reported in the first and second groups in each subfigure of Figure 4, respectively. The mean metrics averaged over major gyral peak nodes are in the third group. On average, major gyral peaks have significantly ($p < .05$, with betweenness of the first age group as the only one exception) higher metric values than the means on the whole brain and gyral crests. In addition, major gyral peaks' graph metrics increase across ages, except for efficiency that changes less.

Finally, we computed the number of different cortical areas in the LVE atlas that are found in the neighbor of a gyral peak. Since many cortical areas in this atlas were suggested to coincide with those in brain functional regions (Lewis and Van Essen 2000), we posited that more cortical areas found around a gyral peak indicate that it might be engaged with more brain functions. It is observed in Figure 5a that gyral peaks are usually found on the borders of cortical areas. These peaks have more cortical areas (L: 3.60 ± 1.68, R: 3.00 ± 1.32) found around their neighborhood (7-order ring neighborhood, r ≈ 1.84 mm) compared to randomly selected vertices on either the whole cortex or the gyral crest (Figure 5b), while the peak–crest difference is not significant on the right hemisphere.
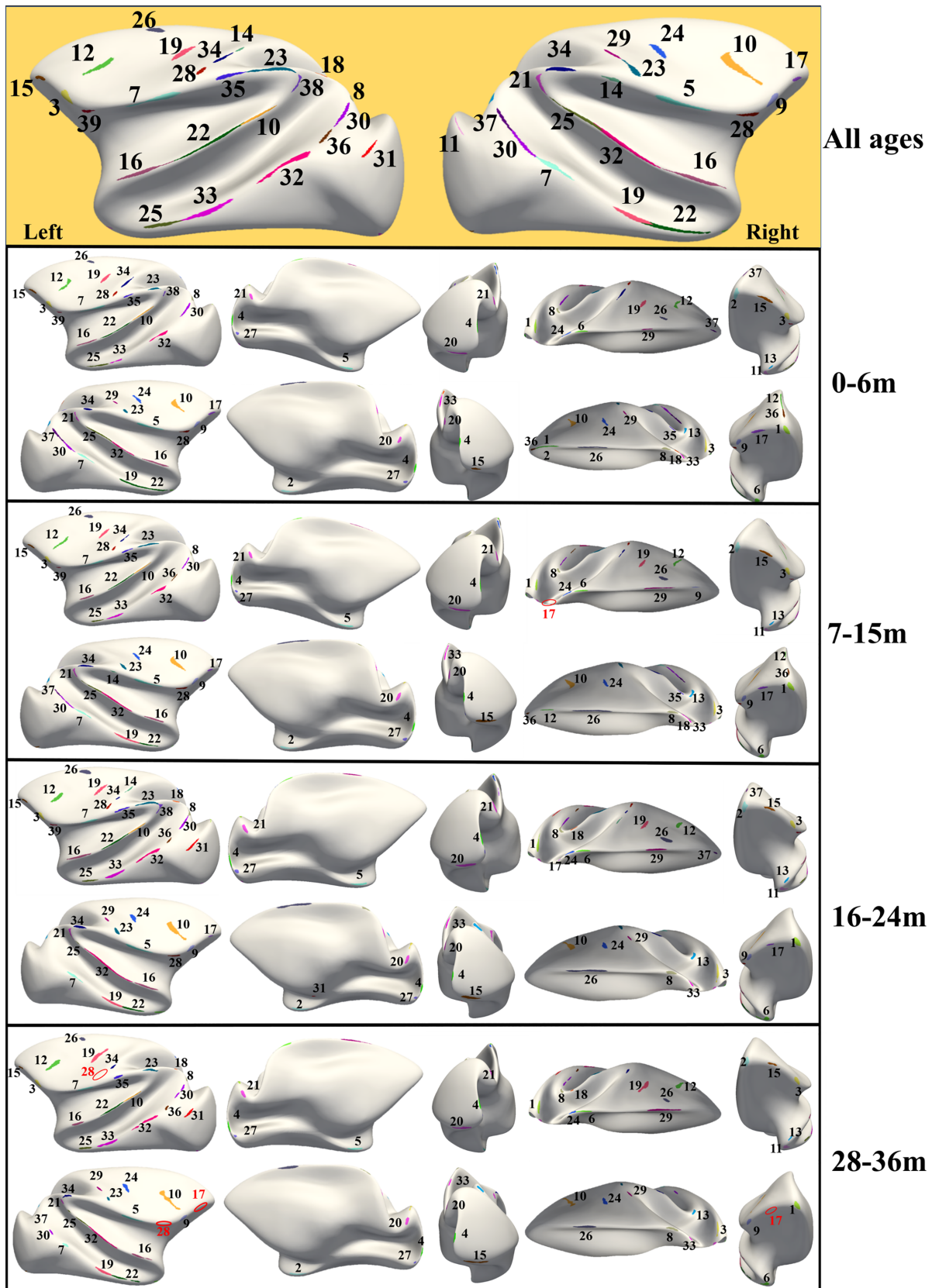
FIGURE 3 Gyral peak clusters in four age groups (0–6 months, 7–15 months, 16–24 months, and 28–36 months). Indices of clusters have longitudinal correspondences. Red indices highlight the clusters identified on the all-age map but not found in an age group. The clusters on all scans in Figure 2d were also shown in the top row as a reference

TABLE 1 Anatomical measures of major gyral peaks across ages. Means (±SD) of these measures as well as those on random tests (1× 10⁴ times) were reported. These random tests provide a null hypothesis distribution to test the significance of the means from major gyral peaks. Recall that the height was normalized to [0, 1]

|		Age 1	Age 2	Age 3	Age 4
Cortical Thickness (mm)					
Major	L	1.34 ± 0.25	1.23 ± 0.26	1.17 ± 0.26	1.15 ± 0.26
	R	1.30 ± 0.23	1.20 ± 0.23	1.15 ± 0.23	1.11 ± 0.24
Random Whole Cortex	L	0.95 ± 0.06	0.89 ± 0.06	0.87 ± 0.06	0.85 ± 0.06
	R	0.93 ± 0.06	0.86 ± 0.06	0.85 ± 0.06	0.84 ± 0.06
Random Gyral Crest	L	1.12 ± 0.09	1.04 ± 0.09	0.87 ± 0.06	0.96 ± 0.09
	R	1.10 ± 0.09	1.02 ± 0.09	0.98 ± 0.09	0.95 ± 0.09
Mean Curvature (mm⁻¹)					
Major	L	0.99 ± 0.24	0.94 ± 0.22	0.93 ± 0.23	0.94 ± 0.24
	R	0.98 ± 0.22	0.92 ± 0.21	0.90 ± 0.22	0.91 ± 0.22
Random Whole Cortex	L	0.04 ± 0.05 0.04 ± 0.05	0.04 ± 0.05 0.04 ± 0.05	0.04 ± 0.05	0.03 ± 0.05
	R			0.04 ± 0.05	0.03 ± 0.05
Random Gyral Crest	L	0.67 ± 0.07	0.66 ± 0.07	0.67 ± 0.07	0.65 ± 0.07
	R	0.70 ± 0.08	0.68 ± 0.07	0.69 ± 0.07	0.68 ± 0.08
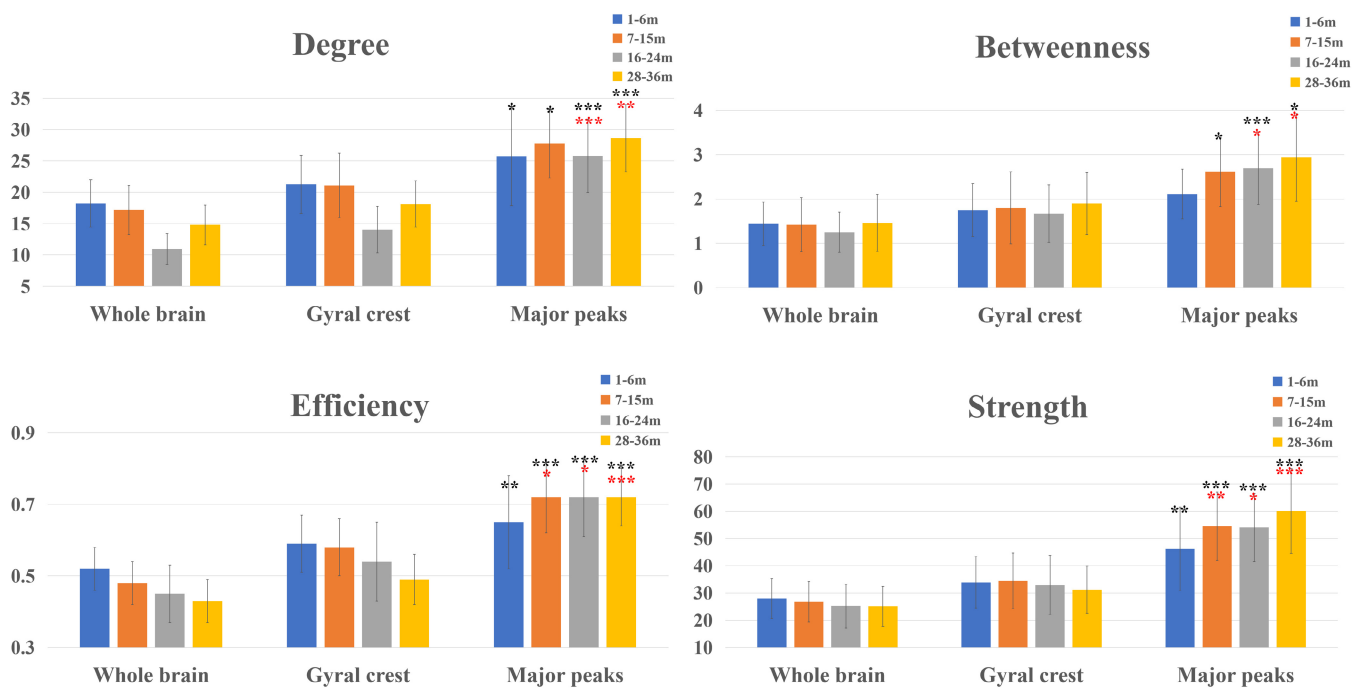
FIGURE 4 Graph metrics of major gyral peaks on structural networks. Random tests (1 ×10⁴ times) were used as the chance line to evaluate whether major gyral peaks have significantly higher metric values than the chance line. Two sets of random tests were performed: One on the whole cortex (p-values were represented by black stars) and the other on the gyral crest (p-values were represented by red stars). * indicates $p < .05$; ** indicates $p < .01$; *** indicates $p < .001$. The error bar represented standard deviation

3.4.3 | Measures on minor peaks

Compared with major peaks, minor peaks are relatively less consistent regarding group-wise peak count and have relatively lower curvature but thicker cortex (Table 2). The difference is not significant for all ($p > .05$).

Minor peaks' cortical thickness decreases with higher amplitude (L: −18.15 ± 6.37%; R: −17.05 ± 5.38%, $p < .05$ for both hemispheres). Curvature decreases with higher amplitude (L: −9.83 ± 11.87%; R: −15.99 ± 10.43%, $p < .05$ for both hemispheres).

Minor peaks have slightly higher graph metric values than those of random tests on whole-brain and gyral crest. However, the difference is
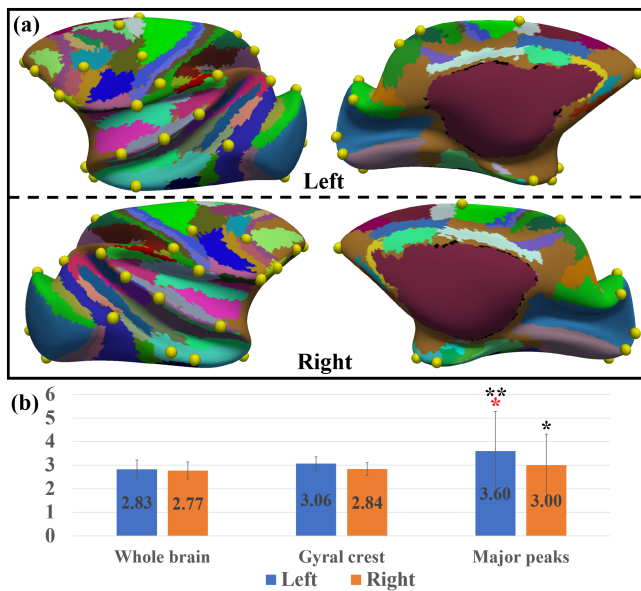
FIGURE 5 (a) Spatial locations of major gyral peaks (yellow bubbles) and their spatial relation with LVE brain atlas; and (b) the number (avg. ± std.) of cortical areas found in the neighborhood (r ≈ 1.84 mm) of major gyral peaks. 1×10^4-time random tests were performed to provide a distribution of null hypothesis that major peaks do not have more cortical areas than random vertices. Two sets of random tests were performed: One on the whole cortex (p-values were represented by black stars) and the other on the gyral crest (p-values were represented by red stars). * indicates $p < .05$; ** indicates $p < .01$

TABLE 2 Anatomical measures of minor gyral peaks across ages. Means (±SD) of these measures were reported. The height was normalized to [0, 1]

	Age1	Age2	Age3	Age4
Cortical Thickness (mm)				
L	1.42 ± 0.19	1.30 ± 0.20	1.23 ± 0.20	1.22 ± 0.20
R	1.30 ± 0.37	1.17 ± 0.35	1.13 ± 0.32	1.07 ± 0.32
Mean Curvature(mm^{-1})				
L	0.98 ± 0.27	0.90 ± 0.21	0.90 ± 0.21	0.89 ± 0.18
R	0.97 ± 0.36	0.87 ± 0.28	0.85 ± 0.26	0.84 ± 0.23

not consistently significant, especially for peak-crest comparison. Minor peaks have slightly more cortical areas in their neighbor (L: 3.42 ± 1.51, R: 3.38 ± 1.19) than both random tests, but there is no significant difference between major peaks and minor peaks. Details are referred to Figures S12, S13 of Supplemental Materials.

3.5 | Spatial patterning of gyral peaks

3.5.1 | Gyral peaks vs. gyral hinges

In our previous works, we defined another group of gyral landmarks (Li et al. 2010), termed gyral hinges, which reside on the crossings of
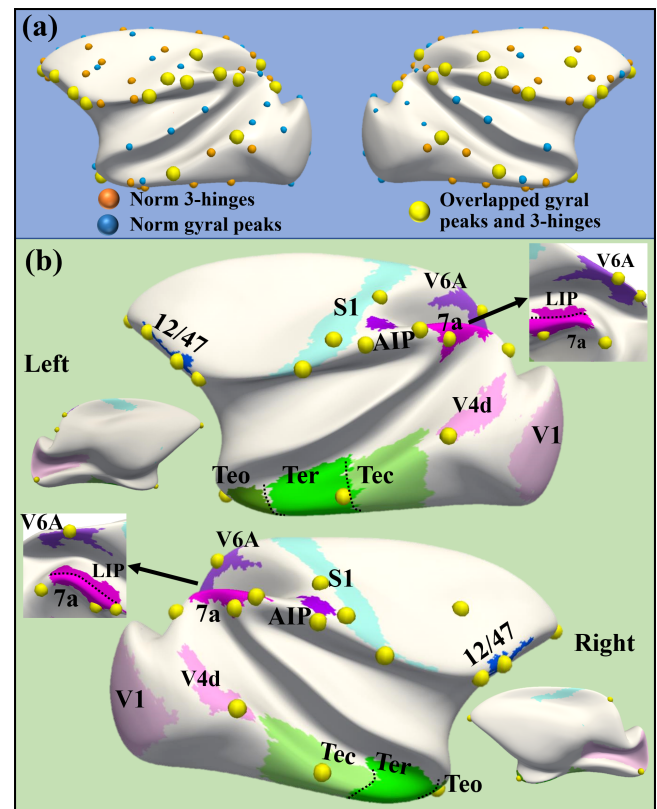

FIGURE 6 (a) Overlapping between gyral hinges and gyral peaks. "Norm" is short for normal, which highlights the gyral hinge or gyral peak with no overlapping with each other. (b) Illustration of the spatial relation between gyral peaks overlapped by gyral hinges (yellow bubbles in (a)) and cortical areas, including the ventral pathway of auditory responsive region (12/47), those on the ventral and dorsal pathway of visual system, and somatosensory regions (S1)

gyri from multiple directions (see examples in Figure S14). Gyral hinges were found to have the thickest cortices, the strongest long-range axonal connections, the most pronounced connectivity diversity, and the most aggregative functional profiles, composing the majority of the cortico-cortical structural connective network's "core" (Li et al. 2010, Yu et al. 2013, Chen et al. 2014, Jiang et al. 2015, Li et al. 2017, Ge et al. 2018, Zhang et al. 2020). It is noted that gyral hinges in Figure 6a are the ones consistent across subjects and ages using a similar pipeline for gyral peak detection. Since gyral peaks were also defined on gyri, we compared the positions of all gyral peaks and gyral hinges and found that some peaks are overlapped with hinges (if the distance is less than 9-order ring neighborhood, r ≈ 2.34 mm and a peak is only assigned to a hinge. Note that the distance between two neighboring gyral crests is 5.70 ± 0.65 mm on the template surface. Therefore, a peak is not likely being overlapped with a hinge on another gyrus), highlighted by yellow bubbles (overlapped peaks, hereafter). Among these overlapped peaks, more major gyral peaks (64.71%) were found than minor ones (40.00%).

It is found that these overlapped peaks are spatially close to brain regions on visual and auditory pathways, including a trans-modal auditory responsive area (12/47) (Romanski 2007), visual areas (V1, V4, V6A, LIP, 7a, and AIP on dorsal pathway, and Teo, Ter, and Tec on

ventral pathway (Freud et al. 2016), as well as the regions in a primary cortex: S1. This result might suggest that these overlapped peaks are spatially placed on a global cortical gradient between the trans-modal cortex and unimodal cortex (Huntenburg et al. 2018). It is noted that there is only one exception, the gyral peak in the frontal pole, which is not close to any of these functional regions.

3.5.2 | Gyral peaks vs. Sulcal pits

It was reported in Lohmann et al. (2008) that sulcal pits form prominent chains stretching from the anterior pole to the posterior pole. The general arrangement of those chains follows the alignment of the lateral ventricle. Such sulcal pit chains were reproduced in macaque

FIGURE 7 Spatial relations among gyral peak chains, sulcal-pit chains, and lateral ventricles. For better visualization, only the centers of major peak clusters in Figure 2 were presented (green bubbles). Yellow bubbles represent the centers of group-wise sulcal pit clusters over all subjects and ages. We empirically identified three chains for gyral peak and two sulcal pit chains. The surfaces of lateral ventricle are shown as references

brains (yellow bubbles and curves in Figure 7). These sulcal pits are the ones consistent across subjects and ages using a similar pipeline for gyral peak detection in this work.

We found that gyral peaks form three chains (green bubbles and curves) of the same orientation as sulcal-pit chains (yellow bubbles and curves). The arrangement of both gyral peak chains and sulcal pit chains all follow the alignment of the lateral ventricle.

We further applied the computational finite element model to investigate the spatial relationship between gyral peaks and sulcal pits. For the details of the computational model check Figure S16 and related texts in Supplemental Materials. In general, we constructed a double-layer cubic model (Figure S16), where the top layer as the cortex grows faster than the bottom layer as the core to mimic the folding process. According to differential tangential growth theory, the cortex as the outer layer of the developing brain grows faster than the core as the inner layer (Richman et al. 1974, Razavi et al. 2015). After a certain amount of growth of the cortex, mechanical instability occurs in the model, and consequently folds form on the cortex (Figure S17). We run 30 models with different initial small perturbations on the surface of the cortex while other parameters were kept the same to have meaningful statistical data. In a real brain, this perturbation could stem from the variation in curvature or heterogeneous growth on distant sites of the brain (Zhang et al. 2016). Initial perturbation in each model was applied as random and small displacements on the nodes of the cortex's surface. The amplitude of the displacements was 0.01 of the cortex thickness (Chavoshnejad et al. 2021). Figure 8 shows the top views of 4 of the 30 models after suppressing the cortex layer.

We found that 42.64 ± 4.20 sulcal pits and 67.11 ± 3.50 gyral peaks were identified in these computational models. The count ratio of gyral peak to sulcal pit is 1.63 ± 0.22, on average. In contrast, the average numbers of sulcal pits, gyral peaks and the ratio are 20.73 ± 3.10, 21.01 ± 2.15 and 0.97 ± 0.16 in macaque brains, respectively. These results suggest that the initial shape could roughly determine the ratio between peaks and pits, since the ratio remains relatively consistent across perturbations in computational models, and cross-subject and -age variabilities in macaque brains. Also, we empirically
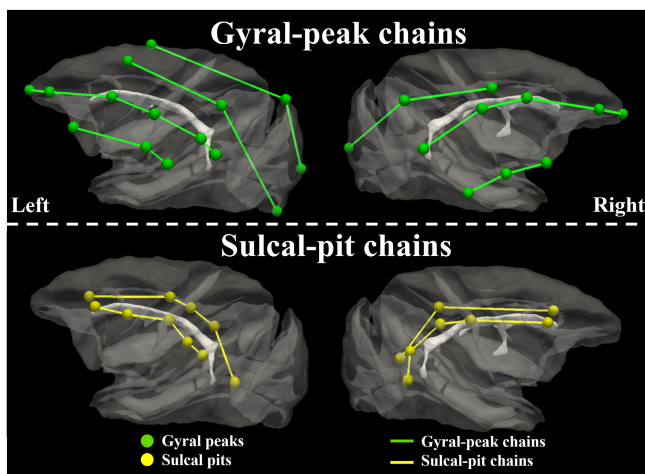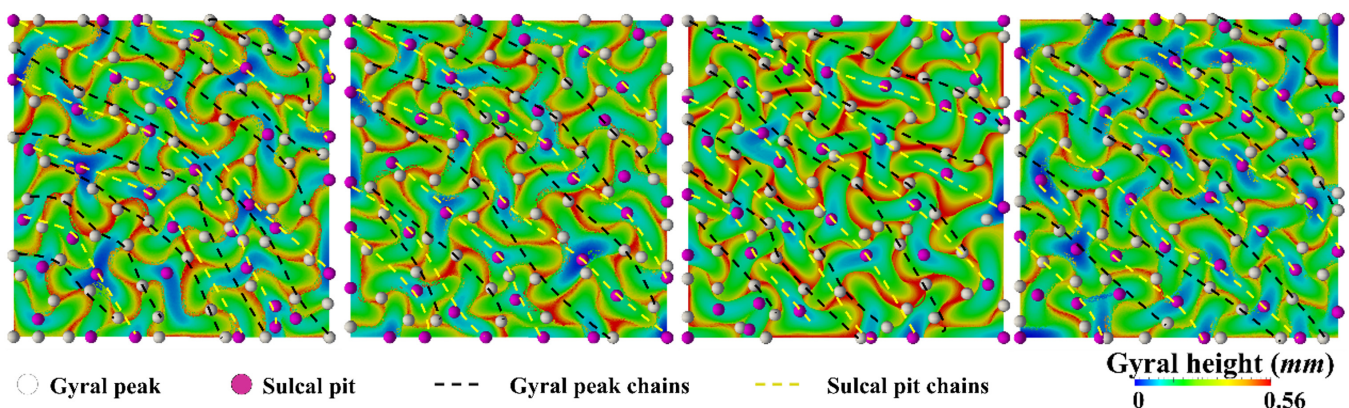

FIGURE 8 Computational models for gyral peaks and sulcal pits. Top views of the highly convoluted cortex with different initial perturbations. Dashed curves highlight the chains of gyral peaks and sulcal pits

identified chains of sulcal pits and gyral peaks which spatially alternate with each other, in the same way as those on macaque brains (Figure 7), suggesting that the emergence of sulcal pits and gyral peaks, as well as their chains, might not be independent of each other.

4 | CONCLUSION AND DISCUSSION

In this work, we defined gyral landmarks, termed gyral peaks, which are the local highest regions on gyri. We studied 156 MRI scans of 32 macaque monkeys with ages ranging from 0 to 36 months and detected 39 and 37 gyral peaks on the left and right hemispheres. We found that: (1) gyral peaks are spatially consistent across individuals; (2) the spatially consistent distributions of gyral peaks are relatively stable during the first 3 years; (3) compared to vertices in other gyral regions, gyral peaks have a thicker cortex and greater mean curvature; (4) the nodal graph metrics on gyral peaks in a dMRI derived structural network, including degree, strength, betweenness, and efficiency, are significantly higher than other nodes including those on gyral crests; (5) gyral peaks are on the borders of structural connectivity parcellations, possibly indicating gyral peaks are involved in more brain functional activities than other brain regions; (6) the gyral peaks overlapping with gyral hinges are distributed on S1 and visual and auditory pathways; (7) gyral peaks form chains and their arrangement follows the alignment of the lateral ventricle in the same way as sulcal pits.

We found that the regularity of gyral peaks is related to the distribution of anatomical and structure wiring features. Major peaks, with higher inter-individual regularity, thinner cortex, and higher curvature compared with minor peaks with lower inter-individual regularity. The longitudinal variation trends of major peaks and minor ones are different in these anatomical and structure measures (see the results in Table 1, Table 2, and Figure 4). Thicker cortex of gyral peaks, compared with one of the other cortical regions including other gyral regions, could be associated with their sharper gyral shapes and stronger axonal connections found in our work, which needs further investigation. The less consistency of minor peaks, most of which are found in temporal lobe, parietal lobe, and frontal lobe, could be explained by the trajectory of development differed across cortical region, where occipital cortex reaches its volume peak at 13 weeks of age and exhibits a continuous decline afterward while the frontal, temporal, and parietal lobes show the protracted growth (Scott et al. 2016). In this sense, ontogenetic factors or the order of development could play a role with later developing lobes, yielding secondary/tertiary cortical folding, including the minor peaks in this work, and being more variable than earlier ones (Fischl et al. 2008).

By comparing our gyral peak related findings with those for sulcal pits in previous reports, we found that they shared similar characteristics in many perspectives. The spatial arrangement of sulcal pits was suggested to be regular across humans in spite of huge cross-subject cortical folding variabilities (Im et al. 2010). Such consistency was also found to be present at term birth and persists in later years in spite of the dramatic expansion of the cortex and deepening of sulci (Meng

et al. 2014). In our work, gyral peaks exhibit similar cross-subject and longitudinal consistency. Although the cortical folding topology of macaque brains is less variable across subjects and ages, our findings suggest a possibility that these gyral landmarks as well as their spatio-temporal consistency can be found in human brains, which is our next research aim. In addition, the arrangement of sulcal pits forms chains, and the arrangement of the sulcal pit chains seem to follow the alignment of the lateral ventricles (Lohmann et al. 2008). The arrangement of gyral peaks forming similar chains interweaved by sulcal pit chains is shown in both brains (Figure 7) and simulation experiments (Figure 8). These findings suggest that gyral peaks and sulcal pits could be produced simultaneously, and might fundamentally be subjected to a related genetic influence.

It is interesting to find that there are overlaps between gyral hinges and gyral peaks. From the mechanical point of view, due to the elasticity and plasticity of brain tissues, gyri and sulci could be the results of the cortical wave development when the outer cortical layer expands faster than the inner one (Bayly et al. 2013). In this sense, gyral hinges could be the results of the interplay of waves from two orientations, since their anatomical appearance is the crossings of gyri from more than two directions. On the other hand, because gyral peaks are the highest cortical locations, they are also expected to be at the locations where peaks of two waves meet and superimpose on each other. Therefore, it is not surprising to find a widely distributed overlap between gyral peaks and gyral hinges, since they could be intrinsically produced by the same mechanical mechanisms (Bayly et al. 2013, Razavi et al. 2015, 2017). However, gyral peaks and hinges do not entirely overlap with each other. Some gyral hinges do not reside on the local maxima of gyral height while some gyral peaks do not reside on the crossing of two gyri. This inconsistency suggests that instability of cortical development (Thoma et al. 2005), usually caused by the faster expansion of the outer layers of the cortex, could not be the only factor to shape the anatomical morphology of cortical folds. Denser fibers connected to gyral hinges reported in our previous work (Ge et al. 2018) could be one of the other factors, in that tension was found along with the orientation of axons (Van Essen 1997, Xu et al. 2010) such that the height of a gyral hinge could be restricted by stronger axonal tension. On the other hand, the elasticity and plasticity of brain tissues as well as degenerative neuronal processes during brain development, such as synaptic pruning (Neniskyte and Gross 2017), possibly lead to the degeneration of some cortical folds, including gyral peaks. One example is "pli de passage" (Gratiolet 1854, Régis et al. 2005, Parent 2014, Mangin et al. 2019), which are pairwise gyri buried in the depth of sulci. In a small group of brains, a continuous gyrus was found to replace the "pli de passage" to literally divide one sulcus into two shorter ones (Régis et al. 2005, Mangin et al. 2019). In this sense, the gyral peaks found on a continuous gyrus and not overlapped with gyral hinges (not on a crossing of gyri from two directions), could be programmed to be crossings of waves at first, but the gyrus from one wave might degenerate for some reasons at last. Based on these discussions above, gyral peaks overlapped by gyral hinges are the "perfect" gyral cortical folds superimposed by two cortical waves in that they reside

on gyri crossings and local height maxima at the same time. More interestingly, these landmarks were found on visual and auditory pathways. Since these pathways exhibit a functional gradient from unimodal regions to trans-modal ones, these anatomical landmarks could offer new insights for the proto-map of the large-scale gradients of brain functions, which were demonstrated to be in line with developmental and genetic gradients on the cortex (Huth et al. 2016, Margulies et al. 2016, Baldassano et al. 2017, Huntenburg et al. 2017, Huntenburg et al. 2018). The timing of cortical development could also be an important factor. It seems that the overlapped landmarks with the closest distance (less than 1 mm) to cortical area borders are more on the higher-order cortex than the normal ones, probably due to that the higher-order cortex has more complicated morphology and develops later than unimodal ones (Sydnor et al. 2021), such that the interplay of folding waves from two orientations yielding the crossings of gyri might account for the higher coincidence between peaks and hinges in these regions.

When relating gyral peaks with structural connective graph metrics, we found that gyral peaks have a higher nodal degree, strength, betweenness, and efficiency in contrast to the mean values on the whole brain and gyral crests, suggesting that they could behave more like hubs of the structural network (Bassett and Bullmore 2006, Bullmore and Sporns 2009, He and Evans 2010). Also, these metrics (except for efficiency) on major gyral peaks increase across ages. It has been reported that the long-range axons and the core of the structural network are present at birth (Dubois et al. 2008, Li et al. 2015, Batalle et al. 2018). In this sense, these results suggest that the role of major gyral peaks as hubs at birth might not be as pronounced as that in adulthood, particularly when compared to other gyral regions. In addition, most gyral peaks are found on the boundary of LVE cortical areas (Figure 5). This finding suggests that gyral peaks could be engaged with more brain functions. Or, they are simply on the borders of these cortical regions, belonging to none of them. Low spatial resolution of macro-scale brain function imaging techniques, such as the functional MRI, may not be able to reveal the functional role of gyral peaks, since the volumetric voxel where a gyral peak resides could cover the multiple functional units such that their activities are blended in one functional signal, making it difficult to determine whether the complex signal of a gyral peak is a result of a blending of multiple sources or reflects its signal-integration nature.

We compared the peak/pit results on macaque brains and those on simulation models. The ratio on macaque brains is around 1 and slightly increases across age groups (age group #1: 0.95 ± 0.16; age group #2: 0.94 ± 0.16; age group #3: 1.00 ± 0.17; age group #4: 1.04 ± 0.12), but the increase is not significant (all neighboring age group difference does not pass t-tests, p-value>.05). This ratio is in line with our empirical hypothesis that peaks and pits could alternate with each other on macaque brains. The slight increase in the peak/pit ratio suggests that the postnatal development of gyri and sulci might not be synchronous. In our recent work (Li et al. 2022), we found on the same dataset that the cortical area expansion is faster on gyral crests than that on sulcal fundi while the depth shrinks faster on sulcal fundi

than that on gyral crests. In this sense, it is hypothesized that gyri might develop later or longer than sulci during the postnatal stage, resulting in a slight increase in peak/pit ratio. Also, the simulation model yields more convoluted gyro-sulcal patterns and a higher peak/pit ratio than the less convoluted macaque cortex. It is thus inferred that the growing complexity of cortical morphology might impose more impact on gyri than sulci. A more concrete investigation of these hypotheses is needed in the future on a prenatal dataset and a multi-species dataset.From the perspective of peak/pit development, it seems that the principal directions of gyri and sulci present a meridian/parallel organization (Toro and Burnod 2003, Régis et al. 2005, Clouchoux et al. 2010, Auzias et al. 2013), which was suggested to result from the principal curvatures of the smooth cortical surface (Tallinen et al. 2016). The periodicity of both sulcal pits and gyral peaks was observed on this organization, which could coincide with gyro-sulcal wavelength. In this sense, sulcal pits and gyral peaks could be the accumulative local minima and maxima where multiple waves superimpose on each other.

Since many deep sulcal pits that are consistent across subjects and invariant across ages were suggested to be the earliest cortical folds (Im et al. 2010), gyral peaks, as morphologically dual patterns, might also appear earlier than other gyral regions. Also, like sulcal pits, higher gyral peaks might also be in place earlier than shallower ones. This postulation deserves further in-depth investigation on the cortex during its fetal stages.

The spatial and temporal coupling between gyral peaks and sulcal pits could be elicited by multiple neuronal processes and associated bio-mechanics. For example, neuron proliferation and migration could be modular in OSVZ, leading to modularized prosperity of neurons in the cortical plate (Stahl et al. 2013). Cortex plate modules with higher neuron popularity were suggested to bulge, making the neighboring modules with neurons less populated buried. Such regionalized proliferation and migration patterns were suggested to give rise to conventional wavy gyro-sulcal patterns. As mentioned above, the landscape of the cortex could be the superimposition of waves of multiple orientations. It is intuitive to postulate that peaks, as maxima of superimposition, might be the region with the highest neuron population, while pits might have the least neuron popularity. Axonogenesis was also suggested to correlate with gyrification (White et al. 2010). In our previous work (He et al. 2021), we suggested that gyral hinges might be coupled with denser and longer axons and possibly more neurons in the cortex to send and receive axonal outputs and inputs. Since gyral hinges are largely overlapped with gyral peaks (Figure 6 in this work), we postulate that gyral peaks could also be connected by denser axons than other gyral regions. On the other hand, co-occurrence of plis de passage gyri and U-shape fibers was suggested in Garcia et al. (2021), while the co-occurrence of plis de passage gyri and sulcal pits wasreported (Mangin et al. 2019) as well. Taken together, it could be possible that U-shape fiber bundles connecting two plis de passage gyri on two neighboring gyri might take the "deepest" U-turn at sulcal pits. Even though the close relationship between axonogenesis and gyrification was partially supported by the synchronous timing of the

emergence of white matter connections and cortical folds (Chi et al. 1977, Huang et al. 2009, White et al. 2010, Takahashi et al. 2012, Dubois et al. 2014, Razavi et al. 2017), the causality between them is still in debate (Garcia et al. 2021). Nevertheless, there still seems to be a consensus that different folding patterns are associated with different axonal wiring patterns. Other development processes, such as the development of intermediate the zone and subplate (Kriegstein et al. 2006, Budday et al. 2015, Duque et al. 2016) and the formation of connections in subcortical tissue (Dehay et al. 2001, Vue et al. 2013, Gamberini et al. 2016, Garcia and Buffalo 2020), were also suggested to contribute to gyrification and worth further attention.

In summary, our definitions and findings of gyral peaks, as well as the relationship between their regularity and multiple anatomical/structural measures provide new clues to explore the neuronal mechanisms of gyrification, such as neurogenesis, migration, axonogenesis, gliogenesis, and myelinogenesis (Chi et al. 1977, Smart et al. 2002, Huang et al. 2009, Takahashi et al. 2010, White et al. 2010, Takahashi et al. 2012, Betizeau et al. 2013, Borrell and Götz 2014, Dubois et al. 2014, Florio and Huttner 2014, Lewitus et al. 2014, Taverna et al. 2014, Hagemeyer et al. 2017, Rash et al. 2019), the underlying genetic mechanisms (Stahl et al. 2013, De Juan Romero and Borrell 2015, Richiardi et al. 2015, Zeng et al. 2015, Krienen et al. 2016) as well as the anatomy-function relationship (Rademacher et al. 1993, Fischl et al. 2008).

CONFLICT OF INTEREST

The authors declare that they have no conflict of interest

DATA AVAILABILITY STATEMENT

The UNC-Wisconsin Rhesus Macaque Neurodevelopment Database (Young et al. 2017) is available as a publicly available dataset.

ORCID

Li Wang https://orcid.org/0000-0003-2165-0080
Tuo Zhang https://orcid.org/0000-0002-6075-3384

REFERENCES

Amunts, K., Malikovic, A., Mohlberg, H., Schormann, T., & Zilles, K. (2000). Brodmann's areas 17 and 18 brought into stereotaxic space-where and how variable? *NeuroImage*, *11*, 66–84.

Andersson, J. L., & Sotiropoulos, S. N. (2016). An integrated approach to correction for off-resonance effects and subject movement in diffusion MR imaging. *NeuroImage*, *125*, 1063–1078.

Auzias, G., Lefèvre, J., Troter, A. L., Fischer, C., Perrot, M., Régis, J., & Coulon, O. (2013). Model-driven harmonic parameterization of the cortical surface: HIP-HOP. *IEEE Transactions on Medical Imaging*, *32*, 873–887.

Baldassano, C., Chen, J., Zadbood, A., Pillow, J. W., Hasson, U., & Norman, K. A. (2017). Discovering event structure in continuous narrative perception and memory. *Neuron*, *95*(3), 709–721.

Barkovich, A. J., Guerrini, R., Kuzniecky, R. I., Jackson, G. D., & Dobyns, W. B. (2012). A developmental and genetic classification for malformations of cortical development: Update 2012. *Brain*, *135*, 1348–1369.

Bassett, D. S., & Bullmore, E. (2006). Small-world brain networks. *The Neuroscientist*, *12*, 512–523.

Batalle, D., Edwards, A. D., & O'Muircheartaigh, J. (2018). Annual research review: Not just a small adult brain: Understanding later neurodevelopment through imaging the neonatal brain. *Journal of Child Psychology and Psychiatry*, *59*, 350–371.

Bayly, P., Okamoto, R., Xu, G., Shi, Y., & Taber, L. (2013). A cortical folding model incorporating stress-dependent growth explains gyral wavelengths and stress patterns in the developing brain. *Physical Biology*, *10*, 16005.

Betizeau, M., Cortay, V., Patti, D., Pfister, S., Gautier, E., Bellemin-Ménard, A., Afanassieff, M., Huissoud, C., Douglas, R. J., & Kennedy, H. (2013). Precursor diversity and complexity of lineage relationships in the outer subventricular zone of the primate. *Neuron*, *80*, 442–457.

Blanton, R. E., Levitt, J. G., Thompson, P. M., Narr, K. L., Capetillo-Cunliffe, L., Nobel, A., Singerman, J. D., McCracken, J. T., & Toga, A. W. (2001). Mapping cortical asymmetry and complexity patterns in normal children. *Psychiatry Research: Neuroimaging*, *107*, 29–43.

Borrell, V., & Götz, M. (2014). Role of radial glial cells in cerebral cortex folding. *Current Opinion in Neurobiology*, *27*, 39–46.

Budday, S., Steinmann, P., III, & Kuhl, E. (2015). Physical biology of human brain development. *Frontiers in Cellular Neuroscience*, *9*, 257.

Bullmore, E., & Sporns, O. (2009). Complex brain networks: Graph theoretical analysis of structural and functional systems. *Nature Reviews Neuroscience*, *10*, 186–198.

Cachia, A., Roell, M., Mangin, J.-F., Sun, Z. Y., Jobert, A., Braga, L., Houde, O., Dehaene, S., & Borst, G. (2018). How interindividual differences in brain anatomy shape reading accuracy. *Brain Structure and Function*, *223*, 701–712.

Chavoshnejad, P., Li, X., Zhang, S., Dai, W., Vasung, L., Liu, T., Zhang, T., Wang, X., & Razavi, M. J. (2021). Role of axonal fibers in the cortical folding patterns: A tale of variability and regularity. *Brain Multiphysics*, *2*, 100029.

Chen, H., X. Yu, X. Jiang, K. Li, L. Li, X. Hu, J. Han, L. Guo, X. Hu & T. Liu. (2014). Evolutionarily-preserved consistent gyral folding patterns across primate brains. In 2014 IEEE 11th International Symposium on Biomedical Imaging (ISBI), 1218–1221. IEEE.

Chi, J. G., Dooling, E. C., & Gilles, F. H. (1977). Gyral development of the human brain. *Annals of Neurology*, *1*, 86–93.

Clark, G. D. (2001). Cerebral gyral dysplasias: Molecular genetics and cell biology. *Current Opinion in Neurology*, *14*, 157–162.

Clouchoux, C., Rivière, D., Mangin, J.-F., Operto, G., Régis, J., & Coulon, O. (2010). Model-driven parameterization of the cortical surface for localization and inter-subject matching. *NeuroImage*, *50*, 552–566.

Cykowski, M. D., Kochunov, P. V., Ingham, R. J., Ingham, J. C., Mangin, J.-F., Rivière, D., Lancaster, J. L., & Fox, P. T. (2008).

Perisylvian sulcal morphology and cerebral asymmetry patterns in adults who stutter. *Cerebral Cortex*, 18, 571–583.

De Juan Romero, C., & Borrell, V. (2015). Coevolution of radial glial cells and the cerebral cortex. *GLIA*, 63, 1303–1319.

Dehay, C., Savatier, P., Cortay, V., & Kennedy, H. (2001). Cell-cycle kinetics of neocortical precursors are influenced by embryonic thalamic axons. *Journal of Neuroscience*, 21, 201–214.

Di Donato, N., Chiari, S., Mirzaa, G. M., Aldinger, K., Parrini, E., Olds, C., Barkovich, A. J., Guerrini, R., & Dobyns, W. B. (2017). Lissencephaly: Expanded imaging and clinical classification. *American Journal of Medical Genetics Part A*, 173, 1473–1488.

Dubois, J., Benders, M., Cachia, A., Lazeyras, F., Ha-Vinh Leuchter, R., Sizonenko, S. V., Borradori-Tolsa, C., Mangin, J.-F., & Hüppi, P. S. (2008). Mapping the early cortical folding process in the preterm newborn brain. *Cerebral Cortex*, 18, 1444–1454.

Dubois, J., Dehaene-Lambertz, G., Kulikova, S., Poupon, C., Hüppi, P. S., & Hertz-Pannier, L. (2014). The early development of brain white matter: A review of imaging studies in fetuses, newborns and infants. *Neuroscience*, 276, 48–71.

Duque, A., Krsnik, Z., Kostović, I., & Rakic, P. (2016). Secondary expansion of the transient subplate zone in the developing cerebrum of human and nonhuman primates. *Proceedings of the National Academy of Sciences*, 113, 9892–9897.

Eickhoff, S. B., Heim, S., Zilles, K., & Amunts, K. (2006). Testing anatomically specified hypotheses in functional imaging using cytoarchitectonic maps. *NeuroImage*, 32, 570–582.

Fernández, V., Llinares-Benadero, C., & Borrell, V. (2016). Cerebral cortex expansion and folding: What have we learned? *The EMBO Journal*, 35, 1021–1044.

Fischl, B., Rajendran, N., Busa, E., Augustinack, J., Hinds, O., Yeo, B. T., Mohlberg, H., Amunts, K., & Zilles, K. (2008). Cortical folding patterns and predicting cytoarchitecture. *Cerebral Cortex*, 18, 1973–1980.

Florio, M., & Huttner, W. B. (2014). Neural progenitors, neurogenesis and the evolution of the neocortex. *Development*, 141, 2182–2194.

Freud, E., Plaut, D. C., & Behrmann, M. (2016). 'What' is happening in the dorsal visual pathway. *Trends in Cognitive Sciences*, 20, 773–784.

Frost, M. A., & Goebel, R. (2012). Measuring structural–functional correspondence: Spatial variability of specialised brain regions after macro-anatomical alignment. *NeuroImage*, 59, 1369–1381.

Gaitanis, J. N., & Walsh, C. A. (2004). Genetics of disorders of cortical development. *Neuroimaging Clinics*, 14, 219–229.

Gamberini, M., Bakola, S., Passarelli, L., Burman, K. J., Rosa, M. G., Fattori, P., & Galletti, C. (2016). Thalamic projections to visual and visuomotor areas (V6 and V6A) in the Rostral Bank of the parieto-occipital sulcus of the Macaque. *Brain Structure and Function*, 221, 1573–1589.

Garcia, A. D., & Buffalo, E. A. (2020). Anatomy and function of the primate entorhinal cortex. *Annual Review of Vision Science*, 6, 411–432.

Garcia, K. E., Wang, X., & Kroenke, C. D. (2021). A model of tension-induced fiber growth predicts white matter organization during brain folding. *Nature Communications*, 12, 1–13.

Ge, F., Li, X., Razavi, M. J., Chen, H., Zhang, T., Zhang, S., Guo, L., Hu, X., Wang, X., & Liu, T. (2018). Denser growing fiber connections induce 3-hinge gyral folding. *Cerebral Cortex*, 28, 1064–1075.

Gratiolet, L. P. (1854). Mémoire sur les Plis cérébraux de l'Homme et des Primatès: *Mit Einem Atlas* (4 pp. XIV pl.) in fol. 33i. A. Bertrand.

Greve, D. N., Van der Haegen, L., Cai, Q., Stufflebeam, S., Sabuncu, M. R., Fischl, B., & Brysbaert, M. (2013). A surface-based analysis of language lateralization and cortical asymmetry. *Journal of Cognitive Neuroscience*, 25, 1477–1492.

Hagemeyer, N., Hanft, K.-M., Akriditou, M.-A., Unger, N., Park, E. S., Stanley, E. R., Staszewski, O., Dimou, L., & Prinz, M. (2017). Microglia contribute to normal myelinogenesis and to oligodendrocyte progenitor maintenance during adulthood. *Acta Neuropathologica*, 134, 441–458.

Hasnain, M. K., Fox, P. T., & Woldorff, M. G. (2001). Structure–function spatial covariance in the human visual cortex. *Cerebral Cortex*, 11, 702–716.

He, Y., & Evans, A. (2010). Graph theoretical modeling of brain connectivity. *Current Opinion in Neurology*, 23, 341–350.

He, Z., Du, L., Huang, Y., Jiang, X., Lv, J., Guo, L., Zhang, S., & Zhang, T. (2021). Gyral hinges account for the highest cost and the highest communication capacity in a corticocortical network. *Cerebral Cortex*, 31, bhab420.

Hinds, O., Polimeni, J. R., Rajendran, N., Balasubramanian, M., Wald, L. L., Augustinack, J. C., Wiggins, G., Rosas, H. D., Fischl, B., & Schwartz, E. L. (2008). The intrinsic shape of human and macaque primary visual cortex. *Cerebral Cortex*, 18, 2586–2595.

Huang, H., Xue, R., Zhang, J., Ren, T., Richards, L. J., Yarowsky, P., Miller, M. I., & Mori, S. (2009). Anatomical characterization of human fetal brain development with diffusion tensor magnetic resonance imaging. *Journal of Neuroscience*, 29, 4263–4273.

Huang, S., Wang, Y., Liang, T., Jin, F., Liu, S., & Jin, Y. (2009). Fabrication and characterization of a novel microparticle with gyrus-patterned surface and growth factor delivery for cartilage tissue engineering. *Materials Science and Engineering: C*, 29, 1351–1356.

Huntenburg, J. M., Bazin, P.-L., Goulas, A., Tardif, C. L., Villringer, A., & Margulies, D. S. (2017). A systematic relationship between functional connectivity and intracortical myelin in the human cerebral cortex. *Cerebral Cortex*, 27, 981–997.

Huntenburg, J. M., Bazin, P.-L., & Margulies, D. S. (2018). Large-scale gradients in human cortical organization. *Trends in Cognitive Sciences*, 22, 21–31.

Huth, A. G., De Heer, W. A., Griffiths, T. L., Theunissen, F. E., & Gallant, J. L. (2016). Natural speech reveals the semantic maps that tile human cerebral cortex. *Nature*, 532, 453–458.

Im, K., Jo, H. J., Mangin, J.-F., Evans, A. C., Kim, S. I., & Lee, J. (2010). Spatial distribution of deep sulcal landmarks and hemispherical asymmetry on the cortical surface. *Cerebral Cortex*, 20(3), 602–611.

Im, K., Choi, Y. Y., Yang, J.-J., Lee, K. H., Kim, S. I., Grant, P. E., & Lee, J.-M. (2011). The relationship between the presence of sulcal pits and intelligence in human brains. *NeuroImage*, 55, 1490–1496.

Im, K., Lee, J.-M., Jeon, S., Kim, J.-H., Seo, S. W., Na, D. L., & Grant, P. E. (2013). Reliable identification of deep sulcal pits: The effects of scan session, scanner, and surface extraction tool. *PLoS ONE*, 8, e53678.

Im, K., Guimaraes, A., Kim, Y., Cottrill, E., Gagoski, B., Rollins, C., Ortinau, C., Yang, E., & Grant, P. E. (2017). Quantitative folding pattern analysis of early primary sulci in human fetuses with brain abnormalities. *American Journal of Neuroradiology*, 38, 1449–1455.

Jenkinson, M., Beckmann, C. F., Behrens, T. E., Woolrich, M. W., & Smith, S. M. (2012). FSL. *NeuroImage*, 62, 782–790.

Jiang, X., Li, X., Lv, J., Zhang, T., Zhang, S., Guo, L., & Liu, T. (2015). Sparse representation of HCP grayordinate data reveals novel functional architecture of cerebral cortex. *Human Brain Mapping*, 36, 5301–5319.

Jiang, X., Zhang, T., Zhang, S., Kendrick, K. M., & Liu, T. (2021). Fundamental functional differences between gyri and sulci: Implications for brain function, cognition, and behavior. *Psychoradiology*, 1, 23–41.

Jin, Y. H., Kiho, I., Yang, J. J., Uicheul, Y., Jong-Min, L., & Bogdan, D. (2013). Automated Sulcal depth measurement on cortical surface reflecting geometrical properties of sulci. *PLoS ONE*, 8, e55977.

Kriegstein, A., Noctor, S., & Martínez-Cerdeño, V. (2006). Patterns of neural stem and progenitor cell division may underlie evolutionary cortical expansion. *Nature Reviews Neuroscience*, 7, 883–890.

Krienen, F. M., Yeo, B. T., Ge, T., Buckner, R. L., & Sherwood, C. C. (2016). Transcriptional profiles of supragranular-enriched genes associate with corticocortical network architecture in the human brain. *Proceedings of the National Academy of Sciences*, 113, E469–E478.

Le Goualher, G., Procyk, E., Collins, D. L., Venugopal, R., Barillot, C., & Evans, A. C. (1999). Automated extraction and variability analysis of sulcal neuroanatomy. *IEEE Transactions on Medical Imaging*, 18, 206–217.

Le Guen, Y., Auzias, G., Leroy, F., Noulhiane, M., Dehaene-Lambertz, G., Duchesnay, E., Mangin, J.-F., Coulon, O., & Frouin, V. (2018). Genetic influence on the sulcal pits: On the origin of the first cortical folds. *Cerebral Cortex*, 28, 1922–1933.

Lewis, J. W., & van Essen, D. C. (2000). Corticocortical connections of visual, sensorimotor, and multimodal processing areas in the parietal lobe of the macaque monkey. *Journal of Comparative Neurology*, *428*, 112–137.

Lewitus, E., Kelava, I., Kalinka, A. T., Tomancak, P., & Huttner, W. B. (2014). An adaptive threshold in mammalian neocortical evolution. *PLoS Biology*, *12*, e1002000.

Li, G., Nie, J., Wu, G., Wang, Y., Shen, D., & Alzheimer's Disease Neuroimaging Initiative. (2012). Consistent reconstruction of cortical surfaces from longitudinal brain MR images. *NeuroImage*, *59*, 3805–3820.

Li, G., Nie, J., Wang, L., Shi, F., Gilmore, J. H., Lin, W., & Shen, D. (2014). Measuring the dynamic longitudinal cortex development in infants by reconstruction of temporally consistent cortical surfaces. *NeuroImage*, *90*, 266–279.

Li, G., Liu, T., Ni, D., Lin, W., Gilmore, J. H., & Shen, D. (2015). Spatiotemporal patterns of cortical fiber density in developing infants, and their relationship with cortical thickness. *Human Brain Mapping*, *36*, 5183–5195.

Li, K., Guo, L., Li, G., Nie, J., Faraco, C., Cui, G., Zhao, Q., Miller, L. S., & Liu, T. (2010). Gyral folding pattern analysis via surface profiling. *NeuroImage*, *52*, 1202–1214.

Li, X., Chen, H., Zhang, T., Yu, X., Jiang, X., Li, K., Li, L., Razavi, M. J., Wang, X., & Hu, X. (2017). Commonly preserved and species-specific gyral folding patterns across primate brains. *Brain Structure and Function*, *222*, 2127–2141.

Li, X., Zhang, S., Jiang, X., Zhang, S., Han, J., Guo, L., & Zhang, T. (2022). Cortical development coupling between surface area and sulcal depth on macaque brains. *Brain Structure and Function*, *227*, 1013–1029.

Lohmann, G., von Cramon, D. Y., & Steinmetz, H. (1999). Sulcal variability of twins. *Cerebral Cortex*, *9*, 754–763.

Lohmann, G., von Cramon, D. Y., & Colchester, A. C. (2008). Deep sulcal landmarks provide an organizing framework for human cortical folding. *Cerebral Cortex*, *18*, 1415–1420.

Mangin, J.-F., Le Guen, Y., Labra, N., Grigis, A., Frouin, V., Guevara, M., Fischer, C., Rivière, D., Hopkins, W. D., Régis, J., & Sun, Z. Y. (2019). "Plis de passage" deserve a role in models of the cortical folding process. *Brain Topography*, *32*, 1035–1048.

Margulies, D. S., Ghosh, S. S., Goulas, A., Falkiewicz, M., Huntenburg, J. M., Langs, G., Bezgin, G., Eickhoff, S. B., Castellanos, F. X., & Petrides, M. (2016). Situating the default-mode network along a principal gradient of macroscale cortical organization. *Proceedings of the National Academy of Sciences*, *113*, 12574–12579.

McKay, D. R., Kochunov, P., Cykowski, M. D., Kent, J. W., Laird, A. R., Lancaster, J. L., Blangero, J., Glahn, D. C., & Fox, P. T. (2013). Sulcal depth-position profile is a genetically mediated neuroscientific trait: Description and characterization in the central sulcus. *Journal of Neuroscience*, *33*, 15618–15625.

Meng, Y., Li, G., Lin, W., Gilmore, J. H., & Shen, D. (2014). Spatial distribution and longitudinal development of deep cortical sulcal landmarks in infants. *NeuroImage*, *100*, 206–218.

Molko, N., Cachia, A., Rivière, D., Mangin, J.-F., Bruandet, M., Le Bihan, D., Cohen, L., & Dehaene, S. (2003). Functional and structural alterations of the intraparietal sulcus in a developmental dyscalculia of genetic origin. *Neuron*, *40*, 847–858.

Morosan, P., Rademacher, J., Schleicher, A., Amunts, K., Schormann, T., & Zilles, K. (2001). Human primary auditory cortex: Cytoarchitectonic subdivisions and mapping into a spatial reference system. *NeuroImage*, *13*, 684–701.

Nakamura, M., Nestor, P. G., McCarley, R. W., Levitt, J. J., Hsu, L., Kawashima, T., Niznikiewicz, M., & Shenton, M. E. (2007). Altered orbitofrontal sulcogyral pattern in schizophrenia. *Brain*, *130*, 693–707.

Neniskyte, U., & Gross, C. T. (2017). Errant gardeners: Glial-cell-dependent synaptic pruning and neurodevelopmental disorders. *Nature Reviews Neuroscience*, *18*, 658–670.

Ono, M., Kubik, S., & Abernathey, C. D. (1990). *Atlas of the cerebral sulci*. Thieme Medical Publishers.

Parent, A. (2014). Louis Pierre Gratiolet (1815-1865) and his contribution to the study of cerebral convolutions in primates. *Neuroscience & Medicine*, *2014*, 1–8.

Rademacher, J., Caviness, V., Jr., Steinmetz, H., & Galaburda, A. (1993). Topographical variation of the human primary cortices: Implications for neuroimaging, brain mapping, and neurobiology. *Cerebral Cortex*, *3*, 313–329.

Rakic, P. (2004). Genetic control of cortical convolutions. *Science*, *303*, 1983–1984.

Rakic, P. (2009). Evolution of the neocortex: A perspective from developmental biology. *Nature Reviews Neuroscience*, *10*, 724–735.

Rash, B. G., Duque, A., Morozov, Y. M., Arellano, J. I., Micali, N., & Rakic, P. (2019). Gliogenesis in the outer subventricular zone promotes enlargement and gyrification of the primate cerebrum. *Proceedings of the National Academy of Sciences*, *116*, 7089–7094.

Razavi, M. J., Zhang, T., Liu, T., & Wang, X. (2015). Cortical folding pattern and its consistency induced by biological growth. *Scientific Reports*, *5*, 1–14.

Razavi, M. J., Zhang, T., Chen, H., Li, Y., Platt, S., Zhao, Y., Guo, L., Hu, X., Wang, X., & Liu, T. (2017). Radial structure scaffolds convolution patterns of developing cerebral cortex. *Frontiers in Computational Neuroscience*, *11*, 76.

Régis, J., Mangin, J. F., Ochiai, T., Frouin, V., Riviére, D., Cachia, A., Tamura, M., & Samson, Y. (2005). "Sulcal root" generic model: A hypothesis to overcome the variability of the human cortex folding patterns. *Neurologia Medico-Chirurgica (Tokyo)*, *45*, 1–17.

Rettmann, M. E., Han, X., Xu, C., & Prince, J. L. (2002). Automated sulcal segmentation using watersheds on the cortical surface. *NeuroImage*, *15*, 329–344.

Richiardi, J., Altmann, A., Milazzo, A.-C., Chang, C., Chakravarty, M. M., Banaschewski, T., Barker, G. J., Bokde, A. L., Bromberg, U., & Büchel, C. (2015). Correlated gene expression supports synchronous activity in brain networks. *Science*, *348*, 1241–1244.

Richman, D. P., Stewart, R., & Caviness, V., Jr. (1974). Cerebral microgyria in a 27-week fetus: An architectonic and topographic analysis. *Journal of Neuropathology & Experimental Neurology*, *33*, 374–384.

Roland, P. E., & Zilles, K. (1998). Structural divisions and functional fields in the human cerebral cortex. *Brain Research Reviews*, *26*, 87–105.

Romanski, L. M. (2007). Representation and integration of auditory and visual stimuli in the primate ventral lateral prefrontal cortex. *Cerebral Cortex*, *Suppl1*, i61–i69.

Scott, J. A., Grayson, D., Fletcher, E., Lee, A., Bauman, M. D., Schumann, C. M., Buonocore, M. H., & Amaral, D. G. (2016). Longitudinal analysis of the developing rhesus monkey brain using magnetic resonance imaging: Birth to adulthood. *Brain Structure & Function*, *221*, 2847–2871.

Shim, G., Jung, W. H., Choi, J.-S., Jung, M. H., Jang, J. H., Park, J.-Y., Choi, C.-H., Kang, D.-H., & Kwon, J. S. (2009). Reduced cortical folding of the anterior cingulate cortex in obsessive–compulsive disorder. *Journal of psychiatry & neuroscience: JPN*, *34*, 443.

Smart, I. H., Dehay, C., Giroud, P., Berland, M., & Kennedy, H. (2002). Unique morphological features of the proliferative zones and postmitotic compartments of the neural epithelium giving rise to striate and extrastriate cortex in the monkey. *Cerebral Cortex*, *12*, 37–53.

Stahl, R., Walcher, T., Romero, C. D. J., Pilz, G. A., Cappello, S., Irmler, M., Sanz-Aquela, J. M., Beckers, J., Blum, R., & Borrell, V. (2013). Trnp1 regulates expansion and folding of the mammalian cerebral cortex by control of radial glial fate. *Cell*, *153*, 535–549.

Stuttered, C. A., & Leventer, R. J. (2014). Polymicrogyria: A common and heterogeneous malformation of cortical development. *American Journal of Medical Genetics Part C: Seminars in Medical Genetics*, *166*, 227–239.

Sun, L., Zhang, D., Lian, C., Wang, L., Wu, Z., Shao, W., Lin, W., Shen, D., Li, G., & UNC/UMN Baby Connectome Project Consortium. (2019). Topological correction of infant white matter surfaces using anatomically constrained convolutional neural network. *NeuroImage*, *198*, 114–124.

Sun, T., & Hevner, R. F. (2014). Growth and folding of the mammalian cerebral cortex: From molecules to malformations. *Nature Reviews Neuroscience*, 15, 217–232.

Sydnor, V. J., Larsen, B., Bassett, D. S., Alexander-Bloch, A., Fair, D. A., Liston, C., Mackey, A. P., Milham, M. P., Pines, A., Roalf, D. R., Seidlitz, J., Xu, T., Raznahan, A., & Satterthwaite, T. D. (2021) Neurodevelopment of the association cortices: Patterns, mechanisms, and implications for psychopathology. *Neuron*, 109, 2820–2846.

Takahashi, E., Dai, G., Wang, R., Ohki, K., Rosen, G. D., Galaburda, A. M., Grant, P. E., & Wedeen, V. J. (2010). Development of cerebral fiber pathways in cats revealed by diffusion spectrum imaging. *NeuroImage*, 49, 1231–1240.

Takahashi, E., Folkerth, R. D., Galaburda, A. M., & Grant, P. E. (2012). Emerging cerebral connectivity in the human fetal brain: An MR tractography study. *Cerebral Cortex*, 22, 455–464.

Tallinen, T., Chung, J. Y., Rousseau, F., Girard, N., Lefèvre, J., & Mahadevan, L. (2016). On the growth and form of cortical convolutions. *Nature Physics*, 12, 588–593.

Taverna, E., Götz, M., & Huttner, W. B. (2014). The cell biology of neurogenesis: Toward an understanding of the development and evolution of the neocortex. *Annual Review of Cell and Developmental Biology*, 30, 465–502.

Thoma, R. J., Yeo, R. A., Gangestad, S. W., Halgren, E., Sanchez, N. M., & Lewine, J. D. (2005). Cortical volume and developmental instability are independent predictors of general intellectual ability. *Intelligence*, 33, 27–38.

Toro, R., & Burnod, Y. (2003). Geometric atlas: Modeling the cortex as an organized surface. *NeuroImage*, 20, 1468–1484.

Tustison, N. J., Avants, B. B., Cook, P. A., Zheng, Y., Egan, A., Yushkevich, P. A., & Gee, J. C. (2010). N4ITK: Improved N3 bias correction. *IEEE Transactions on Medical Imaging*, 29, 1310–1320.

Van Den Heuvel, M. P., & Sporns, O. (2011). Rich-club organization of the human connectome. *Journal of Neuroscience*, 31, 15775–15786.

van den Heuvel, M. P., Kahn, R. S., Goñi, J., & Sporns, O. (2012). High-cost, high-capacity backbone for global brain communication. *Proceedings of the National Academy of Sciences*, 109, 11372–11377.

Van Essen, D. C. (1997). A tension-based theory of morphogenesis and compact wiring in the central nervous system. *Nature*, 385, 313–318.

Van Essen, D. C. (2002). Windows on the brain: The emerging role of atlases and databases in neuroscience. *Current Opinion in Neurobiology*, 12, 574–579.

Van Essen, D. C., & Dierker, D. L. (2007). Surface-based and probabilistic atlases of primate cerebral cortex. *Neuron*, 56, 209–225.

Vue, T. Y., Lee, M., Tan, Y. E., Werkhoven, Z., Wang, L., & Nakagawa, Y. (2013). Thalamic control of neocortical area formation in mice. *Journal of Neuroscience*, 33, 8442–8453.

Wang, F., C. Lian, J. Xia, Z. Wu, D. Duan, L. Wang, D. Shen & G. Li. (2018). Construction of spatiotemporal infant cortical surface atlas of rhesus macaque. In *2018 IEEE 15th international symposium on biomedical imaging (ISBI 2018)*, 704–707. IEEE.

Wang, L., Shi, F., Yap, P. T., Lin, W., Gilmore, J. H., & Shen, D. (2013). Longitudinally guided level sets for consistent tissue segmentation of neonates. *Human Brain Mapping*, 34, 956–972.

Wang, L., Shi, F., Li, G., Gao, Y., Lin, W., Gilmore, J. H., & Shen, D. (2014). Segmentation of neonatal brain MR images using patch-driven level sets. *NeuroImage*, 84, 141–158.

Wang, L., Gao, Y., Shi, F., Li, G., Gilmore, J. H., Lin, W., & Shen, D. (2015). LINKS: Learning-based multi-source IntegratioN frameworK for segmentation of infant brain images. *NeuroImage*, 108, 160–172.

Welker, W. (1990). Why does cerebral cortex fissure and fold? In *Cerebral cortex* (pp. 3–136). Springer.

White, T., Su, S., Schmidt, M., Kao, C.-Y., & Sapiro, G. (2010). The development of gyrification in childhood and adolescence. *Brain and Cognition*, 72, 36–45.

Xia, J., Wang, F., Wu, Z., Wang, L., Zhang, C., Shen, D., & Li, G. (2020). Mapping hemispheric asymmetries of the macaque cerebral cortex during early brain development. *Human Brain Mapping*, 41, 95–106.

Xu, G., Knutsen, A. K., Dikranian, K., Kroenke, C. D., Bayly, P. V., & Taber, L. A. (2010). Axons pull on the brain, but tension does not drive cortical folding. *Journal of Biomechanical Engineering*, 132, 71013.

Yang, F., & Kruggel, F. (2008). Automatic segmentation of human brain sulci. *Medical Image Analysis*, 12, 442–451.

Yeh, F.-C., Wedeen, V. J., & Tseng, W.-Y. I. (2010). Generalized q-sampling imaging. *IEEE Transactions on Medical Imaging*, 29, 1626–1635.

Yeh, F.-C., Verstynen, T. D., Wang, Y., Fernández-Miranda, J. C., & Tseng, W.-Y. I. (2013). Deterministic diffusion fiber tracking improved by quantitative anisotropy. *PLoS ONE*, 8, e80713.

Yeo, B. T., Sabuncu, M. R., Vercauteren, T., Ayache, N., Fischl, B., & Golland, P. (2009). Spherical demons: Fast diffeomorphic landmark-free surface registration. *IEEE Transactions on Medical Imaging*, 29, 650–668.

Young, J. T., Shi, Y., Niethammer, M., Grauer, M., Coe, C. L., Lubach, G. R., Davis, B., Budin, F., Knickmeyer, R. C., & Alexander, A. L. (2017). The UNC-Wisconsin rhesus macaque neurodevelopment database: A structural MRI and DTI database of early postnatal development. *Frontiers in Neuroscience*, 11, 29.

Yu, X., H. Chen, T. Zhang, X. Hu, L. Guo & T. Liu. (2013). Joint analysis of gyral folding and fiber shape patterns. In *2013 IEEE 10th International Symposium on Biomedical Imaging*, 85–88. IEEE.

Zeng, T., Chen, H., Fakhry, A., Hu, X., Liu, T., & Ji, S. (2015). Allen mouse brain atlases reveal different neural connection and gene expression patterns in cerebellum gyri and sulci. *Brain Structure and Function*, 220, 2691–2703.

Zhang, T., Razavi, M. J., Li, X., Chen, H., Liu, T., & Wang, X. (2016). Mechanism of consistent gyrus formation: An experimental and computational study. *Scientific Reports*, 6, 1–11.

Zhang, T., Li, X., Jiang, X., Ge, F., Zhang, S., Zhao, L., Liu, H., Huang, Y., Wang, X., & Yang, J. (2020). Cortical 3-hinges could serve as hubs in cortico-cortical connective network. *Brain Imaging and Behavior*, 14, 1–18.

Zhong, T., Zhao, F., Pei, Y., Ning, Z., Liao, L., Wu, Z., Niu, Y., Wang, L., Shen, D., & Zhang, Y. (2021). DIKA-Nets: Domain-invariant knowledge-guided attention networks for brain skull stripping of early developing macaques. *NeuroImage*, 227, 117649.

Zilles, K., Schleicher, A., Langemann, C., Amunts, K., Morosan, P., Palomero-Gallagher, N., Schormann, T., Mohlberg, H., Bürgel, U., & Steinmetz, H. (1997). Quantitative analysis of sulci in the human cerebral cortex: Development, regional heterogeneity, gender difference, asymmetry, intersubject variability and cortical architecture. *Human Brain Mapping*, 5, 218–221.

Zilles, K., & Palomero-Gallagher, N. (2001). Cyto-, myelo-, and receptor architectonics of the human parietal cortex. *NeuroImage*, 14, S8–S20.

SUPPORTING INFORMATION

Additional supporting information can be found online in the Supporting Information section at the end of this article.